Induced Seismicity in the Dallas-Fort Worth Basin: Enhanced Seismic Catalogue and Evaluation of Fault Slip Potential

Bing Q. Li, Jean-Philippe Avouac and Zachary E. Ross, California Institute of Technology; Jing Du, Total E&P Research and Technology, LLC; Estelle Rebel, Total S.A.*

Summary

We present an updated catalogue of seismicity in the Dallas-Fort Worth basin from 2008 to the end of 2019 using state-of-the-art phase picking and association methods based on machine learning. We then calculate the pore pressure and poroelastic stress changes on a monthly basis between 2000 and 2020 for the whole basin, incorporating fluid injection/extraction histories at 104 saltwater injection and 20576 production wells. These pore pressure and poroelastic stress changes are calculated using coupled analytical solutions for a point source injection in a 3D homogeneous isotropic medium, and are superposed for all wells. We suggest that the poroelastic effects of produced gas and water contribute significantly to fault instability.

Introduction

The Barnett shale formation (‘Barnett’ hereafter) in the Bend-Arch Fort Worth Basin in Northeast Texas is a tight gas reservoir, where hydrocarbon production has greatly benefitted from the development of horizontal drilling and hydraulic fracturing technologies. To date, over 6.2 x 10^{11} m^3 of gas has been extracted from the reservoir. However, significant seismic activity has been detected since 2008 in the Dallas-Fort Worth metroplex which overlies the Barnett (Quinones et al., 2019, DeShon et al., 2019), which has generally been attributed to the large volumes of saltwater injected into the permeable Ellenburger limestone formation underlying the Barnett shale (Zhai et al., 2018). However, there is some evidence (Chen et al., 2020) that the poroelastic stress changes from produced gas and co-produced water contributed to fault instability in the Azle sub-region. Here, we present an updated seismic catalogue, and calculate the pore pressure and poroelastic stress changes over time for the whole basin, incorporating fluid injection/extraction histories at 104 saltwater injection and 20576 production wells. These pore pressure and poroelastic stress changes are calculated using coupled analytical solutions for a point source injection in a 3D homogeneous isotropic medium, and are superposed for all wells.

Method: Seismic Catalogue

Raw waveforms and station data are downloaded from IRIS and TexNet, and include networks 4F, NQ, TA, TX, X9, and ZW (DeShon et al., 2019). We then automatically detect tentative seismic phases on the continuous waveform data using the Generalized Phase Detection (Ross et al., 2018) algorithm, which are trained on waveforms from Southern California but show generally acceptable performance in the study region. The phase detections are then associated to earthquakes using PhaseLink (Ross et al., 2019), which is initially trained using a synthetic dataset of picks intended to replicate the general station geometry and noise characteristics, and then subsequently retrained using a set of real picks. Events are located using NonLinLoc (Lomax et al., 2000). We benchmark our final catalogue against that presented by Quinones et al. (2019), and find that they are relatively similar.

Method: Stress Model

To solve for the change in Coulomb failure stress at points of interest, we first incorporate the 3D isotropic coupled poroelastic model presented by Rudnicki (1986) and subsequently adapted by Segall and Lu (2015), which solves for the pore pressure, *p*, and poroelastic stress change resulting from a single point injector with mass injection rate *q(t)* at the origin as

$$p(\boldsymbol{x},t) = \frac{1}{(4\pi)^{\frac{3}{2}} p_0 r^3} \frac{(\lambda_u - \lambda)(\lambda + 2\mu)}{\alpha^2(\lambda_u + 2\mu)} \int_0^t q(t')\xi^3 e^{-\frac{1}{4}\xi^2} dt' \tag{1}$$

and

$$\sigma_{ij}(\boldsymbol{x},t) = \frac{1}{2\pi p_0 r^3} \frac{\mu(\lambda_u - \lambda)}{\alpha(\lambda_u + 2\mu)} \int_0^t q(t') \left[\delta_{ij}(g - \xi g') + \frac{x_i x_j}{r^2}(\xi g' - 3g) \right] dt' \tag{2}$$

, ξ is the similarity variable defined as

$$\xi(t') = \frac{r}{\sqrt{c(t - t')}} \tag{3}$$

and functions g(ξ) and its derivative g’(ξ) defined as

$$g(\xi) = \operatorname{erf}\left(\frac{1}{2}\xi\right) - \frac{\xi}{\sqrt{\pi}} e^{-\frac{1}{4}\xi^2} \tag{4}$$

$$g'(\xi) = \frac{1}{2\sqrt{\pi}} \xi^2 e^{-\frac{1}{4}\xi^2} \tag{5}$$

Here, μ is the shear modulus, λ and λ_u are the drained and undrained Lamé parameters, x is the position of the receiver, t is time, α is the Biot coefficient, and r is the distance between the source and the receiver. All material properties are listed in Table 1, and are assumed constant throughout the reservoir.

The pore pressure and stress changes are superposed for 104 injection and 20576 production wells within the region of interest, and we calculate the Coulomb stress change as

$$\Delta CFS = \tau + f(\sigma_n + p)$$

Where shear stress τ and normal stress σ_n (positive in extension) are calculated according to the receiver fault orientations listed in Table 2. Note that we consider production wells as negative values of injection, and we additionally assume that the spatial distribution of produced water is the same as produced oil and gas, and scale the co-produced water volume such that the total volume extracted between the years 2000 and 2020 is equivalent to the total volume of saltwater injection in the same time period. Production and injection histories are shown in Figure 1, where the production occurs in the Barnett at approximately 2.1 to 2.2 km depth, and saltwater injection in the Ellenburger at approximately 2.2 to 3.5 km depth (Smye et al., 2019). Note that the poroelastic solution assumes single phase flow, and so mixing between gas and water is not incorporated in our model. We also note that negative values of Coulomb stress change in a tension-positive context may arise from either clamping or a decrease in shear stress on the specific fault geometry.

Table 1: Mechanical and fluid properties used in analysis

Density ρ_0	Water	998 kg/m^3
	Natural Gas	0.82 kg/m^3
Fluid dynamic viscosity η	Water	1.1x10^{-3} Pa.s
	Natural Gas	1.1x10^{-5} Pa.s
Gas compressibility factor Z	Natural Gas	0.88
Shear modulus μ	Ellenburger	30 GPa
Skempton coefficient B	Ellenburger	0.75
Hydraulic diffusivity c	Water	0.13 m^2/s
	Natural Gas	6.41 m^3/s
Drained Poisson's ratio ν	Ellenburger	0.25
Undrained Poisson's ratio ν_u	Ellenburger	0.45
Friction coefficient f	Basement	0.6

Table 2: Fault orientation for each sub-region in the Dallas-Fort Worth basin

	Strike	Dip	Rake
Airport (Ogwari et al., 2018)	240	60	-90
Azle (Chen e al., 2020)	225	70	-90
Cleburne (Justinic et al., 2013)	0	60	-90
Irving (Quinones et al., 2019)	60	60	-90
Venus (Scales et al., 2017)	220	60	-90

Results

Figure 2 shows the outline of the study area, including the locations of high-volume production and saltwater injection wells, as well as the seismometers used to create the catalogued earthquakes. As has been noted in previously noted, the earthquakes are located in five major sub-regions: The Airport sequence, which occurred, between 2008-2010, Azle, which swarmed between 2014-2015, Cleburne, which swarmed 2009-2010 and 2018, Irving, which has experienced seismicity since 2015, and finally Venus which has also experienced significant seismicity since 2015.

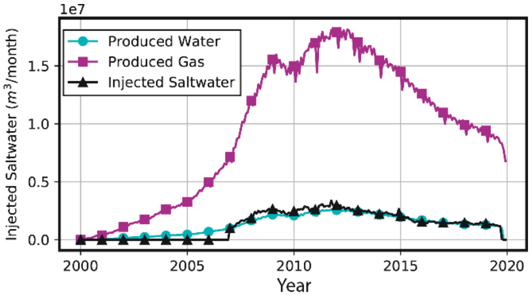

Figure 1: Total extraction and injection rates of natural gas and water at reservoir conditions over time for all Barnett wells.

To assess whether our catalogue contains a statistically significant number of fore- and after-shocks, we apply the nearest-neighbour analysis suggested by Zaliapin and Ben-Zion (2013), which allows separating fore- and aftershocks from independent earthquakes as they cluster closer in normalized time and space, leading to a bi-modal distribution. The results are shown in Figure 3, where we can see that the detected earthquakes fall into a single mode and are as a result unlikely to contain a significant fraction of fore- or after-shocks, which ensures that the majority of the analysed events are not caused by the stress changes related to previous earthquakes.

Figure 4 shows the evolution of pore pressure and poroelastic stress changes at each sub-region over time, as calculated at the centre of the cluster of seismicity, using the analytical solution described in the methods section. The net Coulomb Failure Stress (CFS) change from all sources is also included in the plot. Firstly, we see that the poroelastic stress changes from gas and water production are significant and comparable to that of saltwater disposal in all sub-regions, and thus should be included to estimate stress changes. Additionally, we see that there is a wide range of critical stresses at which failure occurs. For example, the Venus sub-region does not a CFS change <0.1 MPa at the onset of detected seismicity, and reaches a maximum of only 0.03 MPa in late 2009. Our calculation yields negative CFS change for the Azle, Cleburne, and Irving regions, which suggests that our calculation incorrectly balances the different sources of stress change or that the magnitude of CFS change may be not be not the critical indicator of induced seismicity. If we consider the rate-state formulation (*e.g.* Segall and Lu, 2015) for nucleation of fault slip, we may also consider the rate of CFS change, which predicts that a sharp increase of CFS may be related to the onset of seismicity.

This holds for the Airport, Cleburne, and Venus sub-regions, where we see that the increase in seismicity rate coincide with positive CFS rate.

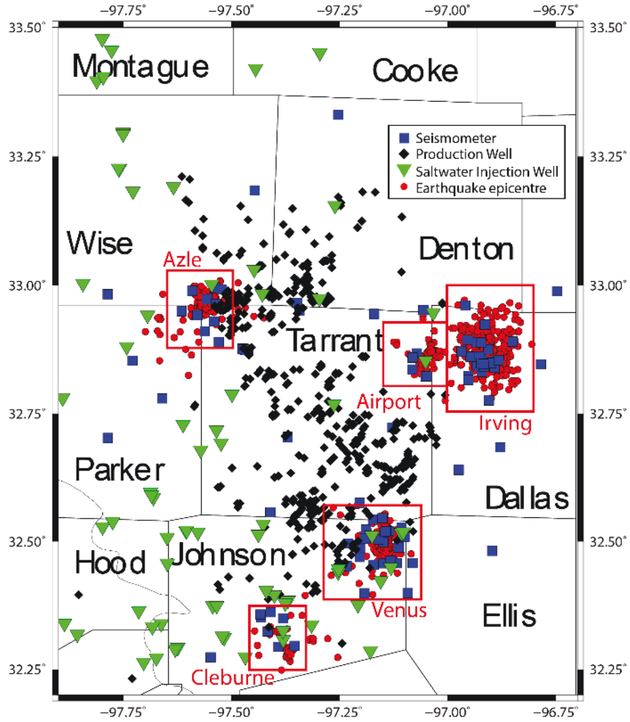

Figure 2: Map of study region, including locations of production and saltwater injection wells totaling greater than 5 x 10^5 m^3 of fluid injection or extraction, seismic stations, and earthquake epicentres. Sub-regions of interest are outlined in red.

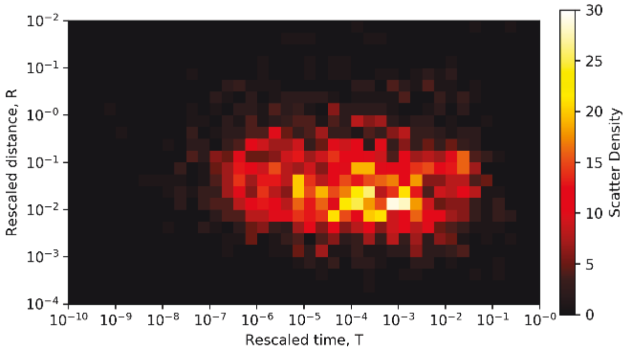

Figure 3: Distribution of spatial and temporal nearest neighbor distances of the Dallas-Fort Worth seismicity.

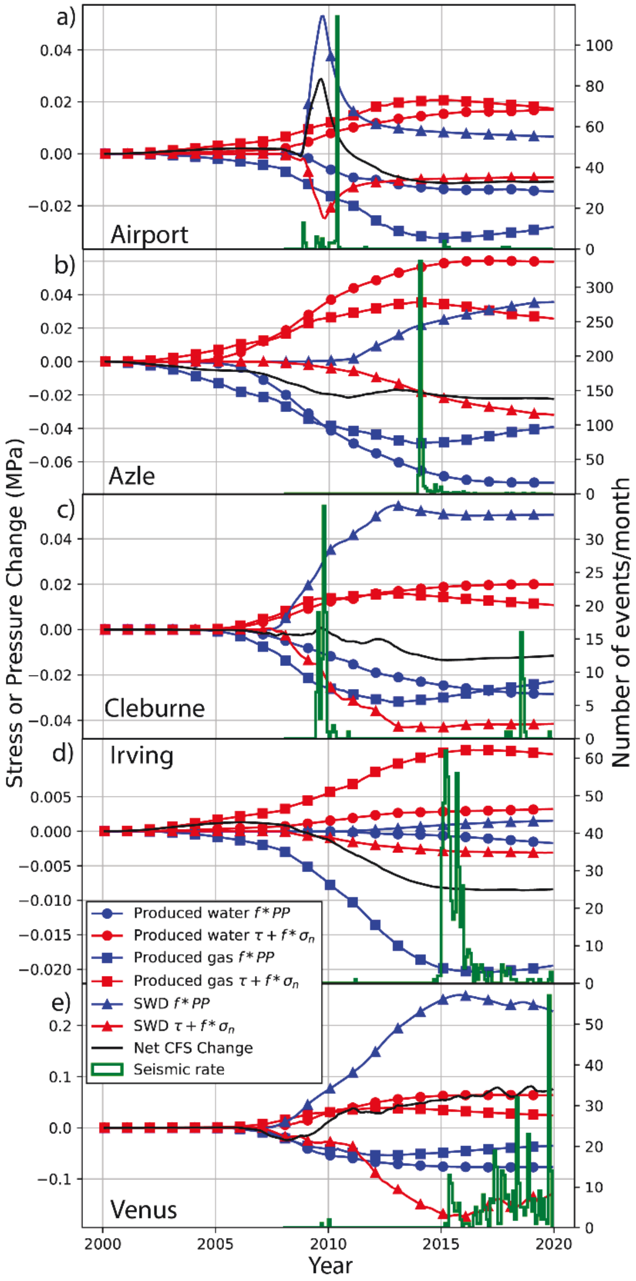

Figure 4: Evolution of pore pressure and poroelastic stress change over time due to produced water, saltwater disposal, and produced gas. Net Coulomb friction stress change is the summation of all sources of stress, shown for a) Airport, b) Azle, c) Cleburne, d) Irving, and e) Venus seismic sequences at an assumed depth of 5 km.

However, the onset of seismicity in the Irving sub-region remains unexplained, since it experiences small negative CFS change and minimal fluctuations in the CFS. It is also interesting that there are sub-regions of the Dallas-Fort Worth basin that experience high CFS changes but exhibit no seismicity, for example the junction of Tarrant-Parker-Johnson-Hood counties, for which the stresses over time are plotted in Figure 5. We can see that the CFS change in this region reach a magnitude of 0.1 MPa and exhibits a sharp increase in 2007, but exhibits no seismicity. This is not for a lack of local faults, for example Hennings et al (2019) notes that there are a number of favourably oriented faults in the vicinity which have not exhibited any slip.

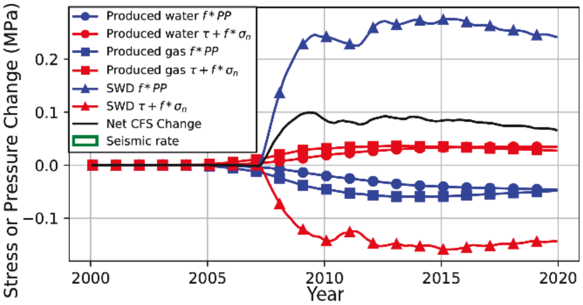

Figure 5: Stress changes at the junction of Tarrant-Parker-Johnson-Hood counties, where no seismicity has been detected

Figure 6 shows the spatial distribution of maximum net Coulomb stress change, alongside the epicenter locations from Figure 2. We see that the saltwater disposal creates higher stress concentrations owing to larger volumes at fewer wells, and the production wells contribute Coulomb stress change over a large area in the basin. We can see that the Azle, Cleburne, and Venus sequences correspond to regions of high Coulomb stress change, however the Airport and Irving sequences do not. We also note, as shown in Figure 5, that there the region of high stress near the junction of Tarrant-Parker-Johnson-Hood counties does not appear to correspond to any detected seismicity.

Conclusions

We present an updated seismic catalogue for the Dallas-Fort Worth basin, and first-order estimates of pore pressure and poroelastic stress changes in each sub-region of detected induced seismicity using analytical solutions. Our results suggest that the stress changes from production may have a significant effect on the Coulomb failure stress on the local faults, and should be accounted for in seismic forecasting. Our results also suggest that there are regions with high stress changes that do not exhibit any induced seismicity, which merit further study.

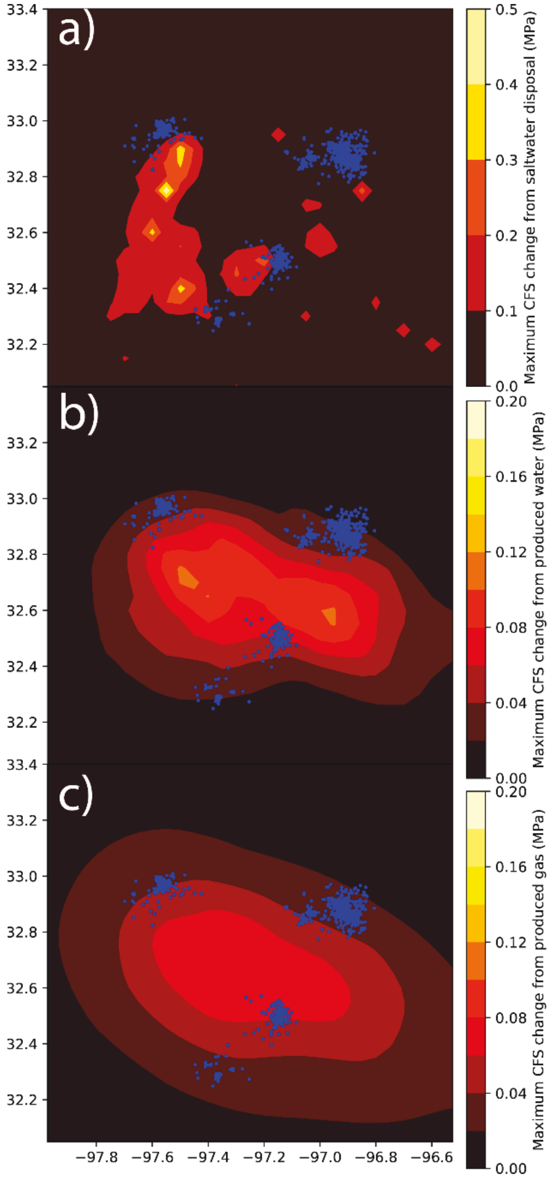

Figure 6: Contour map showing spatial distribution of maximum net Coulomb stress change a) saltwater disposal, b) produced water, and c) produced gas between 2000-2020 at 5 km depth, assuming the DFW airport fault orientation. Earthquake locations are shown in blue.

Acknowledgements

The authors would like to thank Total S.A. for support, David CRIGHTON at Total and Andrea Wu at RS Energy Group for their help on accessing PRISM software and downloading the production data in the study area.